Eur. Phys. J. Appl. Phys. (2013) 64: 24506
DOI: 10.1051/epjap/2013120462

THE EUROPEAN PHYSICAL JOURNAL APPLIED PHYSICS

Regular Article

Numerical simulation of incoherent optical wave propagation in nonlinear fibers*

Arnaud Fernandez[1,2,a], Stéphane Balac[1,2], Alain Mugnier[3], Fabrice Mahé[1,4], Rozenn Texier-Picard[5], Thierry Chartier[1,2], and David Pureur[3]

[1] UEB, Université Européenne de Bretagne, Université de Rennes I, 5 boulevard Laënnec, 35000 Rennes, France
[2] CNRS FOTON (UMR 6082), ENSSAT, 6 rue de Kerampont, BP 80518, 22305 Lannion, France
[3] QUANTEL, 4 rue Louis de Broglie, 22300 Lannion, France
[4] IRMAR (CNRS UMR 6625), Université de Rennes I, Campus de Beaulieu, 35042 Rennes, France
[5] IRMAR (CNRS UMR 6625), ENS Cachan Bretagne, av. Robert Schuman, 35170 Bruz, France

Received: 11 October 2012 / Received in final form: 3 February 2013 / Accepted: 4 February 2013
Published online: 6 November 2013 –

Abstract. The present work concerns the study of pulsed laser systems containing a fiber amplifier for boosting optical output power. In this paper, this fiber amplification device is included into a MOPFA laser, a master oscillator coupled with fiber amplifier, usually a cladding-pumped high-power amplifier often based on an ytterbium-doped fiber. An experimental study has established that the observed nonlinear effects (such as Kerr effect, four waves mixing, Raman effect) could behave very differently depending on the characteristics of the optical source emitted by the master laser. However, it has not yet been possible to determine from the experimental data if the statistics of the photons is alone responsible for the various nonlinear scenarios observed. Therefore, we have developed a numerical simulation software for solving the generalized nonlinear Schrödinger equation with a stochastic source term in order to validate the hypothesis that the coherence properties of the master laser are mainly liable for the behavior of the observed nonlinear effects.

1 Introduction

The MOPFA laser system (Fig. 1) under study aims at the generation of very high-power (10 kW) nanosecond pulses at 532 nm with 50 to 500 kHz repetition rate. This high-power pulsed source originates from successive amplification of a master laser source (seeder) emitted at 1064 nm that will be amplified through a pre-amplification stage and an ytterbium-doped fiber amplifier pumped with a high-power laser diode at 976 nm. Once amplification is done, the high-power pulses cross the frequency doubling stage to produce nanosecond pulses at 532 nm. However, the frequency doubling stage efficiency can be drastically reduced if the amplified pulses spectrum full width at half maximum (FWHM) exceeds a critical value depending on the physical properties of the doubling stage material. Thus, it is necessary to identify which parameters related to the seeder and/or fiber properties mainly affect the spectrum spreading.

An experimental technique presented in reference [1] offered us the possibility to measure, throughout temporal slices of the pulse, the spectral evolution of nonlinear effects such as Kerr effect, four waves mixing, Raman effect, for three different pulsed fiber laser sources (100 ns of temporal width) generated at 1064 nm with a repetition rate of 20 kHz and then amplified by an ytterbium-doped fiber amplifier. Observation of pulse temporal slices of 10 ns of duration at different temporal positions in the pulse was carried out obtained thanks to an acousto-optical modulator located after the amplifier. By using an optical spectrum analyzer it has been possible to characterize the evolution of the nonlinear effects occurring in the fiber amplified pulse and to discriminate between the nonlinear effects associated with each slice of the pulse.

Whatever the choice of the source, the initial profile of the laser pulses were quasi-similar (100 ns of temporal width).

The experimental results show that, for the same intensity pulse temporal profile (same temporal width and peak power), there exist very different nonlinear behaviors depending on whether the source is partially coherent with a narrow spectrum or incoherent with a larger spectrum, that is to say from an experimental viewpoint, depending on the characteristics of the master laser oscillator. However, these experimental observations do not allow us to decide whether the statistics of photons is the only

* Contribution to the Topical Issue "Numelec 2012", Edited by Adel Razek.

[a] e-mail: afernand@laas.fr

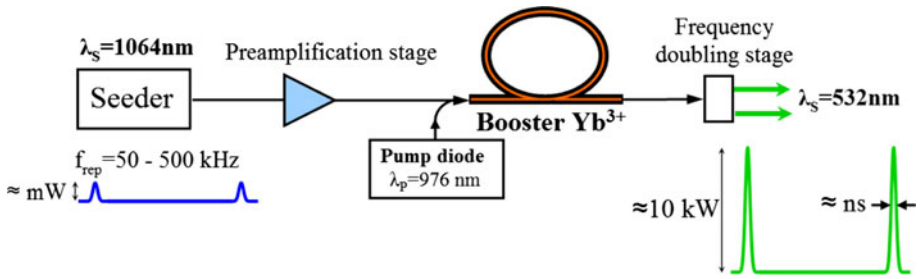

Fig. 1. Schematic of a MOPFA laser with a frequency doubling stage for the generation of high-power nanosecond green pulses at few tens of kHz repetition frequency.

responsible factor for the various nonlinear scenarios. Hence we have developed a numerical simulation software to study the coherence properties of a fiber amplified pulsed laser source in order to resolve the question.

Wave propagation into an optical fiber with group index n_g is governed by the generalized nonlinear Schrödinger equation (GNLSE). This particular form of the Schrödinger equation is obtained from the general set of Maxwell equations taking advantage of a certain number of assumptions made possible from the very specific characteristics of wave propagation in a medium such as a fiber [2]. Among the assumptions that usually can be done for wave propagation into an optical fiber, one is that the optical wave is quasi-monochromatic. It means that the pulse spectrum, centered at pulsation ω_0, is assumed to have a spectral width $\delta\omega$ small compared to ω_0. Another approximation consists in assuming that the optical wave propagates on a single transverse-electric fiber mode and maintains its polarization along the fiber length so that a scalar model (rather than a full vectorial one) is valid. This is not really the case most of the time but however the approximation works quite well in practice [2]. One of the major assumptions, referred to as the *slowly varying envelope approximation*, concerns the expression of the electric field in the optical fiber. It assumes that the electric field $\mathbf{E}$ is linearly polarized along a direction $\mathbf{e}_x$ transverse to the direction of propagation $\mathbf{e}_z$ defined by the fiber axis and can be represented as a function of time T and position $\mathbf{r} = (\mathbf{x}, \mathbf{y}, \mathbf{z})$ as:

$$\mathbf{E}(\mathbf{r}, T) = A(z, T)F(x, y)e^{-\mathrm{i}(\omega_0 T - kz)}\mathbf{e}_x, \tag{1}$$

where $A(z, T)$ represents the slowly varying pulse envelope, $F(x, y)$ is the electric wave transverse representation also termed *modal distribution* and k is the wavenumber. The expression of the modal distribution F can most of the time be computed explicitly using the classical method of separation of variables used for partial differential equations (PDE). For instance, for circular constant transverse section fibers, it can be expressed in terms of Bessel functions [3]. To compute the slowly varying pulse envelope A, it is convenient to introduce a frame of reference, called the *retarded frame*, moving with the pulse at the "group velocity" $v_g = c/n_g$. The relation between the "local time" t in the retarded frame and the absolute time T is given as: $t = T - \frac{z}{v_g}$. If we introduce as new unknown function $A(z, t) = A(z, t + \frac{z}{v_g})$ then in the situation considered in this work, the evolution of A is governed by the following form of the GNLSE [2]:

$$\begin{aligned}\frac{\partial}{\partial z}A(z,t) = &-\frac{\alpha(z)}{2}A(z,t) + \left(\sum_{n=2}^{n_{\max}} i^{n+1}\frac{\beta_n}{n!}\frac{\partial^n}{\partial t^n}A(z,t)\right)\\ &+\mathrm{i}\gamma\left[i_d + \frac{i}{\omega_0}\frac{\partial}{\partial t}\right](A(z,t)((1-f_R)\,|A(z,t)|^2\\ &+f_R\int_0^\infty h_R(\tau)|A(z,t-\tau)|^2\mathrm{d}\tau)),\end{aligned} \tag{2}$$

where i_d denotes the identity operator. The physical effects for wave propagation in fiber taken into account in equation (2) are the following. First, some linear effects are expressed through the linear attenuation/gain coefficient α and the linear dispersion coefficients β_n, $2 \leq n \leq n_{\max}$ where, e.g., β_2 expressed in units ($\mathrm{ps}^2\ \mathrm{km}^{-1}$) accounts for chromatic effects. Nonlinear effects are involved in equation (2) through the nonlinear parameter γ expressed in units ($\mathrm{W}^{-1}\ \mathrm{km}^{-1}$) and defined as $\gamma = \omega_0 n_2(\omega_0)/(cA_{\mathrm{eff}}(\omega_0))$, where n_2 is the nonlinear refractive index for the pulsation ω_0 and A_{eff} known as the effective mode area is defined from the modal distribution $F(x, y)$ as

$$A_{\mathrm{eff}} = \frac{\left(\iint_{\mathbb{R}^2}|F(x,y)|^2\,\mathrm{d}x\mathrm{d}y\right)^2}{\iint_{\mathbb{R}^2}|F(x,y)|^4\,\mathrm{d}x\mathrm{d}y}. \tag{3}$$

In equation (2) first-order partial derivation with respect to time takes into account the dispersion of the nonlinearity through the simplified optical shock parameter $\tau_{\mathrm{shock}} = 1/\omega_0$. Use of the simplified optical shock parameter is relevant when the frequency dependence of the mode effective area A_{eff} defined in equation (3) can be neglected, which is a valid assumption with the fibers used in our study. Instantaneous Kerr effect manifests itself through the term $(1 - f_R)\,|A|^2$. The delayed Raman contribution in the time domain is taken into account through the convolution product between the instantaneous power $|A(z, t)|^2$ and the Raman time response function for silica-core fibers h_R. For silica fibers, an expression for h_R is proposed in reference [4]. The constant f_R represents the fractional contribution of the delayed Raman response to nonlinear polarization. It is found to be about 0.2 [5]. As a first step in this study, we have not taken into account in our model physical phenomena such as amplified spontaneous emission and Raman spontaneous emission.

In order to present our numerical method for solving the GNLSE (2), the following mathematical framework is introduced. We denote by $\mathcal{D}$ the unbounded linear operator:

$$\mathcal{D} : A \mapsto -\frac{1}{2}\alpha A - \sum_{n=2}^{n_{\max}} \beta_n \frac{i^{n-1}}{n!}\partial_t^n A \tag{4}$$

and we introduce the nonlinear operator:

$$\mathcal{N} : A \longmapsto \mathrm{i}\gamma\,\mathcal{T}_t\left[(1-f_r)A|A|^2 + f_r A\,(h_R \star_t |A|^2)\right], \tag{5}$$

where $\star_t$ stands for the convolution operator with respect to the time variable and $\mathcal{T}_t$ refers to the differential operator $i_d + (1/\omega_0)(\partial/\partial t)$. We are then interested in solving the following PDE problem set over the fiber length $[0, L]$:

$$\begin{cases} \frac{\partial}{\partial z}A(z,t) = \mathcal{D}A(z,t) + \mathcal{N}(A)(z,t) & \forall t \in \mathbb{R} \\ A(0,t) = a_0(t) & \forall t \in \mathbb{R}, \end{cases} \tag{6}$$

where in the deterministic case the source term a_0 is assumed to belong to the Hilbert space $\mathbb{L}^2(\mathbb{R}, \mathbb{C})$. This PDE problem is not amenable to analytical solution and the use of numerical approximation techniques is required. Classical numerical methods for solving (6) are based on a split-step Fourier transform approach and among them the symmetric split-step Fourier method (S3F method) is the most widely used [2,6,7]. Recently a "fourth-order Runge-Kutta method in the interaction picture method" (RK4-IP method) has been proposed [8] as a very promising alternative to split-step methods for solving the GNLSE. Both methods (S3F and IP) exhibit a computational inner structure very similar and therefore have a computational cost very comparable, although the IP method has an order 4 convergence rate whereas the S3F method is dependent on the second-order accuracy of Strang splitting formula and possesses a global quadratic convergence rate [9].

In the present work, the incoherence of the master laser source is modeled by the way of stochastic processes. Namely, the source term a_0 is assumed to be a complex Gaussian process. As a statistical analysis over a large number of samples is to be achieved once the pulse has propagated along the fiber to determine the characteristics of the pulse amplitude A at the fiber end, we have chosen to implement the RK4-IP method rather than the S3F one to solve the GNLSE in order to decrease the computation time.

The paper is organized as follows. In Section 2 we briefly present the interaction picture for solving the GNLSE and focus on the way the various terms involved in the GNLSE are computed. We present the algorithm of the RK4-IP method used for the purposes of the numerical study of the coherence properties of a fiber laser and we detail the embedded Runge-Kutta method used for local error estimation and adaptive step-size control. In Section 3 we present the way the existence of an incoherent optical source is taken into account in the simulation software by introducing complex random processes and we detail the numerical difficulties to overcome. In Section 4 we present numerical results obtained with our simulation software and we propose a physical interpretation of the results in the context of the study of coherence properties of a fiber laser.

2 Solving the GNLSE by RK4-IP method

Recently a "fourth-order Runge-Kutta method in the interaction picture method" (RK4-IP method) has been presented in reference [8] together with an experimental comparison of the RK4-IP method to other split-step methods based on their numerical efficiency on benchmark problems in optics. The numerical investigation undertaken in reference [8] indicates that the RK4-IP method exhibits interesting convergence properties and provides more accurate and efficient numerical results than comparable split-step methods. In reference [9] we have investigated the numerical properties of the RK4-IP method from a mathematical point of view; we have exhibited the inner computational structure of the IP method and have compared it to the symmetric split-step method to confirm the numerical comparison results given in reference [8]. We briefly present in this section the RK4-IP method for solving the GNLSE and we emphasize on the computational setting of the method.

2.1 Presentation of the RK4-IP method

2.1.1 A splitting behind the IP method

For numerical purposes, the interval $[0, L]$ corresponding to the fiber length is divided into K subintervals where the spatial grid points are denoted by z_k, $k = \{0, \ldots, K\}$ such that $]0, L] = \cup_{k=0}^{K-1}]z_k, z_{k+1}]$, where $0 = z_0 < z_1 < \cdots < z_{K-1} < z_K = L$. The step length between z_k and z_{k+1} is denoted h_k and we have also set $z_{k+\frac{1}{2}} = z_k + \frac{h_k}{2}$.

The interaction picture method for solving problem (6) consists in solving over each sub-interval $[z_k, z_{k+1}]$ the following three nested problems [9]:

$$\begin{cases} \frac{\partial}{\partial z}A_k(z,t) = \mathcal{D}A_k(z,t) & \forall z \in [z_k, z_k + \frac{1}{2}]\,\forall t \in \mathbb{R} \\ A_k(z_k,t) = A_{k-1}(z_k,t) & \forall t \in \mathbb{R}, \end{cases} \tag{7}$$

where for $k \geq 1$ the mapping $t \in \mathbb{R} \mapsto A_{k-1}(z_k, t)$ represents the solution at grid point z_k computed at the previous step $k-1$ and where for $k = 0$ we have $A_{-1}(z_0, t) = a_0(t) \forall t \in \mathbb{R}$,

$$\begin{cases} \frac{\partial}{\partial z}A_k^{\mathrm{ip}}(z,t) = \mathcal{G}_k(z,t,A_k^{\mathrm{ip}}) & \forall z \in [z_k, z_{k+1}]\,\forall t \in \mathbb{R} \\ A_k^{\mathrm{ip}}(z_k,t) = A_k(z_{k+\frac{1}{2}},t) & \forall t \in \mathbb{R}, \end{cases} \tag{8}$$

where $t \in \mathbb{R} \mapsto A_k(z_{k+\frac{1}{2}}, t)$ represents the solution to problem (7) at point $z_{k+\frac{1}{2}}$ and

$$\begin{cases} \frac{\partial}{\partial z}A_k(z,t) = \mathcal{D}A_k(z,t) & \forall z \in [z_{k+\frac{1}{2}}, z_{k+1}]\,\forall t \in \mathbb{R} \\ A_k(z_k,t) = A_k^{\mathrm{ip}}(z_{k+1},t) & \forall t \in \mathbb{R}, \end{cases} \tag{9}$$

where $t \mapsto A_k^{\mathrm{ip}}(z_{k+1}, t)$ represents the solution to problem (8) at grid point z_{k+1}. In problem (8), we have set

$$\mathcal{G}_k(z, t, \cdot) = \exp(-(z - z_{k+\frac{1}{2}})\mathcal{D}) \circ \mathcal{N} \circ \exp((z - z_{k+\frac{1}{2}})\mathcal{D}),$$

where the exponential terms have to be understood in the sense of the continuous group generated by the unbounded linear operator $\mathcal{D}$.

Solving the sequence of three nested problems (7)–(9) over the interval $[z_k, z_{k+1}]$ can be interpreted as doing a change of unknown to solve problem (6) over $[z_k, z_{k+1}]$ taking as new unknown the mapping [9]:

$$A_k^{\mathrm{ip}} : (z, t) \in [z_k, z_{k+1}] \times \mathbb{R} \mapsto \exp(-(z - z_{k+\frac{1}{2}})\mathcal{D}) \times A_k(z, t).$$

This viewpoint has the advantage of showing why the IP method has better convergence properties than split-step based methods. Contrary to the latter methods where the split-step scheme introduces an approximation corresponding to a truncation in the Bakker-Hausdorf formula, with the IP method the splitting being exact since it corresponds to a change of unknown.

The major interest in doing such a change of unknown is that contrary to problem (6), problem (8) for the unknown A_k^{ip} does not involve explicitly partial derivation with respect to the time variable t and therefore can be numerically solved using standard quadrature schemes for ordinary differential equations such as Runge-Kutta methods. Partial derivation with respect to time now occurs through the operators $\exp(\pm(z - z_{k+\frac{1}{2}})\mathcal{D})$ that can be computed in a very efficient way by means of Fourier transforms.

We now detail the way the three problems (7), (8) and (9) are solved numerically.

2.1.2 Solving the nonlinear problem (8)

Problem (8) can be numerically solved by using a standard quadrature scheme for ordinary differential equations such as the fourth-order Runge-Kutta (RK4) scheme defined by the Butcher tableau [10].

$$\begin{array}{c|cccc} 0 & & & & \\ \frac{1}{2} & \frac{1}{2} & & & \\ \frac{1}{2} & 0 & \frac{1}{2} & & \\ 1 & 0 & 0 & 1 & \\ \hline & \frac{1}{6} & \frac{1}{3} & \frac{1}{3} & \frac{1}{6} \end{array} \tag{10}$$

This Runge-Kutta method is known to have convergence order 4. One step of the RK4 scheme is used to approach the solution to problem (8) at grid point z_{k+1} as follows:

$$A_k^{\mathrm{ip}}(z_{k+1}, t) \approx A_k^{\mathrm{ip}}(z_k, t) + \frac{h_k}{6}\left(\alpha_1 + 2\alpha_2 + 2\alpha_3 + \alpha_4\right),$$

where

$$\begin{aligned}
\alpha_1 &= \mathcal{G}_k\left(z_k, t, A_k^{\mathrm{ip}}(z_k, t)\right) \\
&= \exp\left(\frac{h_k}{2}\mathcal{D}\right) \times \mathcal{N}\left(\exp\left(-\frac{h_k}{2}\mathcal{D}\right) \times A_k^{\mathrm{ip}}(z_k, t)\right) \\
\alpha_2 &= \mathcal{G}_k\left(z_k + \frac{h_k}{2}, t, A_k^{\mathrm{ip}}(z_k, t) + \frac{h_k}{2}\alpha_1\right) \\
&= \mathcal{N}\left(A_k^{\mathrm{ip}}(z_k, t) + \frac{h_k}{2}\alpha_1\right) \\
\alpha_3 &= \mathcal{G}_k\left(z_k + \frac{h_k}{2}, t, A_k^{\mathrm{ip}}(z_k, t) + \frac{h_k}{2}\alpha_2\right) \\
&= \mathcal{N}\left(A_k^{\mathrm{ip}}(z_k, t) + \frac{h_k}{2}\alpha_2\right) \\
\alpha_4 &= \mathcal{G}_k\left(z_k + h_k, t, A_k^{\mathrm{ip}}(z_k, t) + h_k\alpha_3\right) \\
&= \exp\left(-\frac{h_k}{2}\mathcal{D}\right) \times \mathcal{N}\left(\exp\left(\frac{h_k}{2}\mathcal{D}\right)\right. \\
&\quad \left. \times A_k^{\mathrm{ip}}(z_k, t) + h_k\alpha_3\right).
\end{aligned}$$

It appears clearly in these formulae that the choice of the point $z_{k+1/2}$ in the initial condition of problem (7) reduces the number of computations of exponential operators, hence the number of Fourier transforms.

2.1.3 Solving the linear problems (7) and (9)

The solution to the linear PDE problem (7) in point $z_{k+\frac{1}{2}}$ can formally be written as [9]:

$$\forall t \in \mathbb{R} \quad A_k(z_{k+\frac{1}{2}}, t) = \exp\left(\frac{h_k}{2}\mathcal{D}\right) A_k(z_k, t),$$

where the exponential term has to be understood in the sense of the continuous group generated by the unbounded linear operator $\mathcal{D}$. The mapping $t\mathbb{R} \mapsto A_k(z_{k+\frac{1}{2}}, t)$ can be computed very efficiently by means of Fourier transform according to the formula:

$$\exp\left(\frac{h_k}{2}\mathcal{D}\right) \times A_k(z_k, t) = \mathcal{F}^{-1}\left[\nu \mapsto \hat{A}_k(z_k, \nu) e^{\hat{d}_\nu \frac{h_k}{2}}\right](t),$$

where $\hat{A}_k(z_k, \cdot)$ denotes the Fourier transform of $A_k(z_k, \cdot)$, $\hat{d}_\nu = -\frac{1}{2}\alpha + \mathrm{i}\sum_{n=2}^{n_{\max}} \frac{\beta_n}{n!}(2\pi\nu)^n$ and $\mathcal{F}^{-1}$ denotes the inverse Fourier transform operator. The solution to the linear PDE problem (9) at grid point z_{k+1} can also be obtained in a very similar way.

2.1.4 Computation of the nonlinear terms

In using the RK4 method for solving problem (8), one needs to compute the nonlinear term (see Eq. (5)):

$$\begin{aligned}
\mathcal{N}(A)(z, t) = \mathrm{i}\gamma \left[\mathrm{id} + \frac{1}{\omega_0}\frac{\partial}{\partial t}\right] \left((1 - f_r)A(z, t)|A(z, t)|^2\right. \\
\left. + f_r A(z, t)\left(h_R(t) \star_t |A(z, t)|^2\right)\right).
\end{aligned}$$

This can be achieved in a very efficient way by means of the Fourier transform again since time derivation of functions is then reduced to multiplying the Fourier transform of the function by a factor $-2i\pi\nu$. To compute $h_R(t) \star_t |A(z,t)|^2$, we use as well the properties of the Fourier transform with respect to convolution as follows:

$$h_R(t) \star_t |A(z,t)|^2 = \mathcal{F}^{-1}[\nu \mapsto \hat{h}_R(\nu) \times \widehat{|A(z,.)|^2}(\nu)](t).$$

Finally, computation of $\mathcal{N}(A)(z,t)$ for all $t \in \mathbb{R}$ and $z \in \mathbb{R}^+$ can be achieved through the following steps:

- Compute the Fourier transforms $\hat{h}_R$ and $\widehat{|A(z,.)|^2}$ of h_R and $t \mapsto |A(z,t)|^2$ respectively.
- Multiply these two mappings and compute the inverse Fourier transform of the result to obtain the mapping $(z,t) \mapsto h_R(t) \star_t |A(z,t)|^2$.
- Compute the Fourier transform of the mapping $t \mapsto (1-f_r)A(z,t)|A(z,t)|^2 + f_r A(z,t)(h_R \star_t |A(z,t)|^2)$.
- Multiply the result by the mapping $\nu \mapsto \mathrm{i}\gamma\left(1 - \frac{2i\pi\nu}{\omega_0}\right)$
- compute the inverse Fourier transform of this last product.

2.1.5 Algorithm of the RK4-IP method

Putting altogether the computational elements given above and after optimizing the whole computational procedure (in particular in order to reduce the number of Fourier transforms to be achieved), we obtain the following algorithm for solving the PDE problem 6 by the RK4-IP method.

RK4-IP algorithm

Input: Array u contains the sampling of the signal amplitude at step k
Array $[\nu_j]_{j=1,\ldots,J}$ contains the frequency sampling points
Array $[z_k]_{k=0,\ldots,K}$ contains the spatial grid points
Array $\widehat{h}_R$ contains the Fourier transform of the Raman response function
{Initialisation}
for $j = 1, \ldots, J$ **do**
  $\widehat{d}[j] \leftarrow -\frac{1}{2}\alpha + \mathrm{i}\sum_{n=2}^{n_{\max}} \frac{\beta_n}{n!}(2\pi\nu_j)^n$
  $tfexpd[j] \leftarrow \exp(\frac{h}{2}\widehat{d}[j])$
end for
$\widehat{u}_1 \leftarrow \mathrm{FFT}(u, forward)$
{Loop over the propagation sub-intervals}
for $k = 1, \ldots, K$ **do**
  for $j = 1, \ldots, J$ **do**
    $\widehat{u}_{ip}[j] \leftarrow tfexpd[j] \times \widehat{u}_1[j]$
  end for
  $\widehat{\alpha}_1 \leftarrow \mathrm{COMPUTE\_TFN}(u)$
  for $j = 1, \ldots, J$ **do**
    $\widehat{\alpha}_1[j] \leftarrow tfexpd[j] \times \widehat{\alpha}_1[j]$
    $\widehat{u}_2[j] \leftarrow \widehat{u}_{ip}[j] + \frac{h}{2}\widehat{\alpha}_1[j]$
  end for
  $u_2 \leftarrow \mathrm{FFT}(\widehat{u}_2, backward)$
  $\widehat{\alpha}_2 \leftarrow \mathrm{COMPUTE\_TFN}(u_2)$
  for $j = 1, \ldots, J$ **do**
    $\widehat{u}_3[j] \leftarrow \widehat{u}_{ip}[j] + \frac{h}{2}\widehat{\alpha}_2[j]$
  end for
  $u_3 \leftarrow \mathrm{FFT}(\widehat{u}_3, backward)$
  $\widehat{\alpha}_3 \leftarrow \mathrm{COMPUTE\_TFN}(u_3)$
  for $j = 1, \ldots, J$ **do**
    $\widehat{u}_4[j] \leftarrow tfexpd[j] \times (\widehat{u}_{ip}[j] + h\widehat{\alpha}_3[j])$
  end for
  $u_4 \leftarrow \mathrm{FFT}(\widehat{u}_4, backward)$
  $\widehat{\alpha}_4 \leftarrow \mathrm{COMPUTE\_TFN}(u_4)$
  for $j = 1, \ldots, J$ **do**
    $\widehat{u}_1[j] \leftarrow tfexpd[j] \times (\widehat{u}_{ip}[j] + \frac{h}{6}\widehat{\alpha}_1[j] + \frac{h}{3}\widehat{\alpha}_2[j] + \frac{h}{3}\widehat{\alpha}_3[j]) + \frac{h}{6}\widehat{\alpha}_4[j]$
  end for
  $u \leftarrow \mathrm{FFT}(\widehat{u}_1, backward)$ {Array u contains the values $[A_k(z_{k+1}, t_j)]_{j=1,\ldots,J}$ the sampling of the signal amplitude at step z_k}
end for

FUNCTION $\widehat{g}$ = COMPUTE_TFN(f)
{Compute the Fourier transform of $g : t \mapsto \mathcal{N}(f)(z,t)$ for a given z}
Input: Array f contains the time sampling of function f for the given z
Array $\widehat{h}_R$ contains the sampled Fourier transform of the Raman response function
Array $[\nu_j]_{j=1,\ldots,J}$ contains the frequency sampling points
Output: Array $\widehat{g}$ contains the sampled Fourier transform of g
for $j = 1, \ldots, J$ **do**
  $op_1[j] \leftarrow |f[j]|^2$
end for
$\widehat{op}_1 \leftarrow \mathrm{FFT}(op_1, forward)$
for $j = 1, \ldots, J$ **do**
  $\widehat{op}_2[j] \leftarrow \widehat{op}_1[j] \times \widehat{h}_R[j]$
end for
$op_2 \leftarrow \mathrm{FFT}(\widehat{op}_2, backward)$ {Array op_2 contains the convolution product $h_R \star_t |f(t)|^2$}
for $j = 1, \ldots, J$ **do**
  $op_3[j] \leftarrow f[j] \times \left((1-f_R)op_1[j] + f_R op_2[j]\right)$
end for
$\widehat{op}_3 \leftarrow \mathrm{FFT}(op_3, forward)$
for $j = 1, \ldots, J$ **do**
  $\widehat{g}[j] \leftarrow \mathrm{i}\gamma(1 + \frac{\nu[j]}{\nu_0})h_t \times \widehat{op}_3[j]$
end for

In this algorithm, the computational cost mainly lies in the computation of the Fourier transforms. Over one spatial step, the number of Fourier transforms to be computed is 16. The C program we have developed to solve the GNLSE (2) by the RK4-IP method according to the above algorithm uses the FFTW library for computing the Fourier transforms [11]. FFTW, for "Fastest Fourier Transform in the West", is a software library for computing discrete Fourier transforms (DFTs) developed by Matteo Frigo and Steven G. Johnson at the Massachusetts Institute of Technology. It supports a variety of algorithms

and it can choose the one it estimates or measures to be preferable in the particular circumstances. FFTW is known as the fastest free software implementation of the Fast Fourier transform (FFT) algorithm at present time. It can compute transforms of real-valued and complex-valued arrays of arbitrary size n with a complexity in $\mathcal{O}(n\log(n))$.

2.2 Embedded Runge-Kutta method for local error estimation

Any numerical method for solving the GNLSE will perform poorly if the approximate solution is computed on a mesh grid with a constant step h. Ideally the step-size between two successive grid points should be selected automatically to maintain the error lower than a given value in order to achieve both reliability and efficiency of the computations. There are several ways to estimate the local error done in each point of the mesh grid and to select a value for the size of the next step. The most common and general way to estimate the local error is by a process known as "step doubling". To estimate the local error, this method requires for each step the computation of a coarse solution and a fine solution obtained by dividing by 2 the step-size used for the coarse solution. This way to estimate the local error is accountable for an over computational cost of around 50% more than the same method without local error estimate for the same accuracy of the computations. A cheaper adaptive step-size method dedicated to the GNLSE is propounded in reference [12]. It is based on the conservation of a physical quantity termed "the optical photon number" during the propagation of an electromagnetic field along a fiber when linear attenuation and Raman scattering in the fiber are neglected. It is therefore possible to calculate the "photon number error", which is related to the local error, at each step of the computation to retrieve information about the numerical error over one computational step of the IP method applied to GNLSE. The interest of this approach, specific to GNLSE for lossless fibers, is that the computation of the photon number error can be done at a very cheap numerical cost. The interest of this approach is that the computation of the photon number error can be done at a very cheap numerical cost. However strictly speaking this method is only valid for lossless fibers or for linear losses fibers.

When using Runge-Kutta methods an alternative way to compute the local error, well documented in the literature on RK methods where it is referred to as the "embedded Runge-Kutta methods" exists, see, e.g., [10]. This way of estimating the local error, inherent to the RK methods themselves, does not require any assumption on the model and is not liable for extra computational cost. It is this method we have chosen to implement in our simulation software. A detailed theoretical and experimental comparison of the three above-mentioned approaches for local error estimation has been achieved and is presented in reference [13].

2.2.1 Principle of embedded Runge-Kutta methods

In this work we have chosen to estimate the local error by using an embedded Runge-Kutta method [10]. Embedded Runge-Kutta (ERK) methods are special Runge-Kutta (RK) methods designed to deliver two approximations of the solution of the initial value problem under consideration corresponding to two RK schemes of different convergence orders. These two approximations of the solution can be considered as an accurate approximate solution (the one computed with the numerical scheme of higher order) and a coarse approximate solution (the one computed with the one of lower order). For efficiency, the two RK schemes bear several computational stages in common in order to reduce the computational cost of the local error estimation. Here we have considered the ERK method given in one hand by the fourth-order RK scheme (RK4) defined by Butcher tableau (10) and on the other hand by the third-order RK scheme (RK3) defined by the following Butcher tableau:

$$\begin{array}{c|cccc|c} 0 & & & & & \\ \frac{1}{2} & \frac{1}{2} & & & & \\ \frac{1}{2} & 0 & \frac{1}{2} & & & \\ 1 & 0 & 0 & 1 & & \\ \hline 1 & \frac{1}{6} & \frac{1}{3} & \frac{1}{3} & \frac{1}{6} & \\ \hline & \frac{1}{6} & \frac{1}{3} & \frac{1}{3} & \frac{1}{15} & \frac{1}{10} \end{array} \tag{11}$$

where the cells highlighted in gray are shared with Butcher tableau (10) for the standard RK4 method. This embedded RK4(3) method actually coincides with Dormand and Prince *Runge-Kutta 4(3) T* method [14].

Assuming that the solution value at grid point z_k is regarded as exact (because we are concerned by an estimation of the local error), we denote by $A_{k+1}^{[3]}$ (resp. $A_{k+1}^{[4]}$) the approximate solution computed at the current grid point z_{k+1} by the third-order (resp. the fourth-order) Runge-Kutta method. The local errors for each of the two methods are respectively given by

$$\begin{aligned} A(z_{k+1},t) - A_{k+1}^{[3]}(t) &= \psi_3(t,z_k,A_k^{[3]})\,h_k^4 + \mathcal{O}(h_k^5), \\ A(z_{k+1},t) - A_{k+1}^{[4]}(t) &= \psi_4(t,z_k,A_k^{[4]})\,h_k^5 + \mathcal{O}(h_k^6), \end{aligned} \tag{12}$$

where ψ_3 (resp. ψ_4) is a function of the *elementary differentials* of order 4 (resp. 5) [10] of the function $\mathcal{G}_k$ involved in problem (7). Therefore by difference of these two relations we obtain:

$$A_{k+1}^{[4]}(t) - A_{k+1}^{[3]}(t) = \psi_3(t,z_k,A_k^{[3]})\,h_k^4 + \mathcal{O}(h_k^5). \tag{13}$$

Thus from (12) and (13) the local error for the RK3 method at grid point z_{k+1} can be approximated with an error in $\mathcal{O}(h_k^5)$ in the following way:

$$\ell_{k+1}(t) \approx A_{k+1}^{[4]}(t) - A_{k+1}^{[3]}(t). \tag{14}$$

The advantages of estimating the local error through the ERK4(3) method defined by Butcher tableau (11) compared to other embedded RK schemes are the following.

The ERK4(3) method preserves all the nice features of the RK4 scheme when used with the IP method as described in Section 2.1.2. Moreover, the computation of both terms $A_{k+1}^{[4]}$ and $A_{k+1}^{[3]}$ in the ERK4(3)-IP method can be achieved at no extra cost compared to the RK4-IP method without local error estimation (namely, the extra cost for each step is negligible since it is limited to two additions and three multiplications and the need to keep in memory two intermediate results). The implementation of the ERK4(3)-IP method requires little modification of the RK4-IP algorithm presented in Section 2.1.5 and we refer to [15] for a comprehensive presentation of the ERK4(3)-IP algorithm.

Finally, the $\mathbb{L}^2$-local error at grid point z_{k+1} is computed as follows:

$$\|\ell_{k+1}\|_{\mathbb{L}^2} \approx \left(\int_{\mathbb{R}} \left| A_{k+1}^{[4]}(t) - A_{k+1}^{[3]}(t) \right|^2 \, \mathrm{d}t \right)^{\frac{1}{2}} \approx \left(h_t \sum_{j=0}^{J-1} \left| A_{k+1}^{[4]}(t_j) - A_{k+1}^{[3]}(t_j) \right|^2 \right)^{\frac{1}{2}}, \quad (15)$$

where $(t_j)_{j=0,\ldots,J}$ denotes a constant step-size sampling h_t of the observed time period and the last approximation results from the use of the left rectangle quadrature rule. We want to mention that even though the local error estimation (14) strictly holds only for the third-order method, in practice we use the value given by the fourth-order method as the approximation of the solution at grid point z_k. In general, it slightly overestimates the actual local error, which is safe but not fully optimal.

2.2.2 Step-size control

For step-size control, a tolerance is given as a bound for the norm of the local error estimation. One step-size control strategy [10] consists in rejecting the current step-size if it gives an estimated local error higher than the specified tolerance and in accepting the solution computed with this step-size otherwise. When the current step-size is rejected, a new smaller step-size has to be chosen to recompute the solution over the current step. Moreover when the current step-size meets the tolerance requirement for the local error, it has to be scaled up for the next step computations. In both cases, the new step-size has to be estimated using the available information on the previous step computations.

For robustness purposes, the step-size control has to be designed in order to respond as smoothly as possible with real or apparent abrupt changes in behavior. This means that the step-size should not vary from one step to the other by an excessive ratio. In order to avoid situations where the specified tolerance is ever exceeded resulting in rejecting too many steps, a safety factor is introduced. If h is the value of the step-size estimated to give a predicted truncation error equal to the tolerance, then the smaller value 0.9 h is used instead. Following these requirements, the step-size control formula proposed in reference [10] reads

$$h_{\text{new}} = \max\left(0.5,\ \min\left(2.0\ ,\ 0.9\left(\frac{\text{tol}}{\text{est}}\right)^{\frac{1}{3}}\right)\right) h_{\text{old}},$$

where "tol" denotes the tolerance value specified by the user as a bound of the local error and "est" denotes the estimation of the local error for the current step computed from (15). The three constants with values 0.5, 2.0 and 0.9 are somewhat arbitrary and have to be regarded as design parameters.

3 Simulation of incoherent laser sources by random process

In this work we have chosen to model the incoherence behavior of the optical source by using random processes following in this a seminal work of Gross and Manassah [16]. Thus the electric field amplitude A is now considered as a complex random process $A_{z,t}$ indexed by the space variable $z \in [0, L]$ and by the time variable $t \in \mathbb{R}$.

3.1 Complex random processes

The electric field amplitude A is a complex random process indexed by the set $[0, L] \times \mathbb{R}$ over a probability space $(\Omega, \mathcal{F}, \mathbb{P})$; that is to say A is now considered as a mapping from the sample space Ω into a set of functions from $[0, L] \times \mathbb{R}$ into $\mathbb{C}$,

$$A : \varpi \in \Omega \mapsto \big(A_\varpi : (z, t) \in [0, L] \times \mathbb{R} \mapsto A(z, t, \varpi) \in \mathbb{C}\big).$$

The value of A at time t and position z for one observed "experiment" is a complex number. When the experiment is repeated, this value is assumed to vary randomly according to the marginal probability distribution of the process. The random process A involves two types of variables, one "probabilistic" variable corresponding to an outcome ϖ in the sample space Ω and one "deterministic" variable $(z, t) \in [0, L] \times \mathbb{R}$ and

- for every fixed outcome $\varpi_0 \in \Omega$, the function $A_{\varpi_0} : (z, t) \in [0, L] \times \mathbb{R} \mapsto A(z, t, \varpi_0) \in \mathbb{C}$ is a "deterministic" function in the usual sense;
- for every fixed value $(z_0, t_0) \in [0, L] \times \mathbb{R}$, the function $A_{z_0,t_0} : \varpi \in \Omega \mapsto A(z_0, t_0, \varpi) \in \mathbb{C}$ is a random variable.

Moreover, for a fixed value $z_n \in [0, L]$, the mapping

$$A^{[z_n]} : \varpi \in \Omega \mapsto \big(A_\varpi^{[z_n]} : t \in \mathbb{R} \mapsto A(z_n, t, \varpi) \in \mathbb{C}\big),$$

is itself a complex random process.

The mean function of the complex random process $A^{[z_n]}$ is defined as

$$m_{A^{[z_n]}} : t \in \mathbb{R} \mapsto \mathbb{E}(A_{z_n,t}) \in \mathbb{C},$$

where $\mathbb{E}$ denotes the expectation function. When it has a sense, the variance of the complex random process $A^{[z_n]}$ is defined by

$$\mathrm{Var}_{A^{[z_n]}} : t \in \mathbb{R} \mapsto \mathbb{E}\big(|A_{z_n,t} - \mathbb{E}(A_{z_n,t})|^2\big) \in \mathbb{R}^+.$$

The covariance function of $A^{[z_n]}$ is the mapping

$$\mathrm{Cov}_{A^{[z_n]}} : (t_1, t_2) \in \mathbb{R}^2 \mapsto \mathbb{E}\big((A_{z_n,t_1} - \mathbb{E}(A_{z_n,t_1}))\,\overline{(A_{z_n,t_2} - \mathbb{E}(A_{z_n,t_2}))}\big).$$

In this study we have assumed for all $z_n \in [0, L]$ the complex random process $A^{[z_n]}$ to be weak-sense (or wide-sense) stationary that is to say its mean function is identically constant and its covariance function is translation invariant, i.e., $\forall \tau \in \mathbb{R}$, $\forall (t_1, t_2) \in \mathbb{R}^2$

$$\mathrm{Cov}_{A^{[z_n]}}(t_1 + \tau, t_2 + \tau) = \mathrm{Cov}_{A^{[z_n]}}(t_1, t_2).$$

For such random processes the covariance function actually only depends on the gap between the two variables rather than on the values of these variables themselves and it is usual to call covariance function of the process the mapping $\mathrm{C}_{A^{[z_n]}} : t \in \mathbb{R} \mapsto \mathrm{Cov}_{A^{[z_n]}}(t, 0)$ instead of the function $\mathrm{Cov}_{A^{[z_n]}}$ itself. The covariance function $\mathrm{C}_{A^{[z_n]}}$ is positive definite.

3.2 Distribution of the source random process

The source field amplitude $A_{0,t}$ is assumed to be a zero mean stationary Gaussian complex random process defined by its covariance function $\Gamma = \mathrm{C}_{A^{[z_0]}}$ that is to say we assume $\forall n \in \mathbb{N}^*$, $\forall (t_1, \ldots, t_n) \in \mathbb{R}^n$ the n dimensional complex random vector $(A_{0,t_1}, \ldots, A_{0,t_n})$ has a zero mean multivariate Gaussian distribution $\mathcal{N}(0, \Sigma)$ where the covariance matrix Σ has entries elements $\Sigma_{ij} = \Gamma(t_i - t_j)$.

3.2.1 Basic ideas of the simulation approach

From a mathematical point of view it is impossible to predict the law of the random process $A_{z,t}$ at any position z in the fiber due to the nonlinearities in the propagation equation (2). We therefore have to restrict ourselves to the computation of the mean and correlation functions of the random process $A_{L,t}$ at the fiber end.

The basic idea of the simulation approach is to randomly draw an outcome $A_{0,t}(\varpi)$ for the source electric field amplitude and to use the propagation equation (2) to compute the electric field amplitude $A_{z,t}(\varpi)$ at any position z along the optical fiber and at any time t. If a large number of outcomes are considered simultaneously, then by statistical averaging it is possible to compute an approximation of the mean and correlation functions of the random process $A_{L,t}$.

Once the time interval has been sampled with a constant time step h_t and discrete times $t_j = j\,h_t$, $j \in \{0, \ldots, J\}$ have been introduced, the continuous zero mean circular stationary Gaussian complex random process $A_{0,t}$ is handled through a zero mean Gaussian complex random vector $\mathbf{X} = (X_{t_0}, \ldots, X_{t_j})$ where the random variable X_{t_j} is defined by $X_{t_j} = A_{0,t_j}$. The elements of the covariance matrix Σ of the random vector $\mathbf{X}$ are given by $\Sigma_{ij} = \Gamma(t_j - t_i)$ and the covariance matrix is hermitian positive definite and Toeplitz. To simulate a multivariate Gaussian distribution $\mathcal{N}(0, \Sigma)$, one can proceed as follows. Let $\mathbf{Y} = (Y_0, \ldots, Y_J)$ be a random vector where the vector components $Y_j, j \in \{0, \ldots, J\}$ are independent normal random variables $\mathcal{N}(0, 1)$ and let $\mathrm{L} \in \mathcal{M}_{J+1}(\mathbb{C})$ be the unique nonsingular lower triangular matrix with positive diagonal entries such that $\Sigma = \mathrm{L}\,\mathrm{L}^{\mathrm{H}}$ (such a Cholesky factorization exists since the covariance Σ is Hermitian positive definite and the matrix L is referred to as the square root of Σ and denoted $\Sigma^{\frac{1}{2}}$). Then the random vector $\mathbf{X} = \mathrm{L}\mathbf{Y}$ has a multivariate Gaussian distribution with covariance matrix Σ and zero mean. Due to the intrinsic dynamic of the propagation equation (2) in the experimental situation considered here, it is necessary to have a time discretization (or correspondingly a frequency one) with a large number of grid points. Indeed, the pulse-width of the studied laser is close to a nanosecond with a spectral width covering few THz at fiber output due to strong occurrence of nonlinearities (self-phase modulation, Raman scattering) through propagation. Hence, for a spectral resolution allowing a spectral accuracy close to the laser longitudinal modes spacing (≈10 MHz), the number of grid points should be as high as 2^{23}.

3.2.2 Generation of the source Gaussian complex random vector

In their work on modeling the propagation of incoherent laser sources in nonlinear fibers [16], Gross and Manassah used the "factorization method" for generating Gaussian complex random vectors based on the Cholesky decomposition of the covariance matrix presented above. The main drawback of this numerical method is that the Cholesky decomposition of the covariance matrix Σ may fail for numerical reasons. Indeed although the covariance matrix Σ is hermitian positive definite, and the Cholesky decomposition exists, in practice for covariance matrices of large size, their smallest eigenvalues decay very rapidly toward 0 and the covariance matrix is almost singular. From a numerical point of view, the covariance matrix Σ is therefore hermitian positive but not definite and the numerical implementation of the Cholesky method fails to compute the Cholesky decomposition of the covariance matrix Σ. This kind of behavior is observed, for instance, for Gaussian correlation functions $\Gamma(t) = a\,\mathrm{e}^{-bt^2}$. Moreover, this method requires $\mathcal{O}(J^2)$ numerical operations to generate one outcome of a Gaussian vector of size J and hence it is computationally expensive for large values of J. In the 1990s alternative numerical methods to the "factorization method" have been investigated for the simulation of large samples according to a multivariate Gaussian distribution. A method of choice is the "circular embedding method" (CEM) independently invented by Dietrich and Newsam [17] and Wood and Chan [18]. The CEM is the

fastest algorithm for unconditional simulation and it is "exact in principle" which means that it is exact under the assumptions that no error in the computer arithmetic occurs and that truly independent random variables are used.

The idea behind the CEM for simulating a zero mean multivariate Gaussian random vector is the following. The covariance matrix Σ which has the property of being a Toeplitz matrix is embedded in a hermitian circulant matrix $\mathrm{C} \in \mathcal{M}_K(\mathbb{C})$. Calculation of the square root $\mathrm{C}^{\frac{1}{2}}$ of a circulant nonnegative definite matrix may be performed efficiently using the Fast Fourier Transform [17,18]. Moreover if $\mathbf{Y} = (Y_1, \ldots, Y_K)$ is a random vector where the components $Y_k, k \in \{1, \ldots, K\}$ are independent normal random variables $\mathcal{N}(0,1)$, then the circulant matrix can be constructed in such a way that a selected sub-vector $X \in \mathbb{C}^{J+1}$ of $Z = \mathrm{C}^{\frac{1}{2}} Y \in \mathbb{C}^K$ has a multivariate Gaussian distribution with covariance matrix Σ and zero mean [17,18]. The algorithm of the CEM can be found in reference [19]. In this work we use the adaptation of the CEM for complex Gaussian random vector [20].

3.3 Statistical analysis of the final complex random vector

As mentioned before, the distribution law of the random process $A_{L,t}$ at the fiber end cannot be predicted by the theory from the distribution law of the source random process $A_{0,t}$. We therefore restrict ourselves to statistical estimation of its mean and correlation functions from a large number M of outcomes $A_{L,t}(\varpi)$. As the mean of a stationary random process is time invariant, we may estimate the mean of $A_{L,t}$ by the cumulative formula

$$m_L \approx \frac{1}{M} \frac{1}{J+1} \sum_{j=0}^{J} \sum_{m=1}^{M} A_{L,t_j}(\varpi_m).$$

The covariance matrix Σ_L of the complex random vector $(A_{L,t_j})_{j=0\cdots,J}$ is hermitian and has upper triangular entries $(j \geq i)$ given by

$$\begin{aligned} \Sigma_{ij} &= \mathbb{E}(A_{L,t_i} \overline{A_{L,t_j}}) - m_L^2 = \Gamma(t_j - t_i) - m_L^2 \\ &= \Gamma((j-i)\, h_t) - m_L^2, \end{aligned}$$

where for all $k \in \{0, \ldots, J\}$

$$\Gamma(k\, h_t) \approx \frac{1}{M} \frac{1}{J-k} \sum_{j=0}^{J-k} \sum_{m=1}^{M} A_{L,t_j}(\varpi_m)\, \overline{A}_{L,t_{j+k}}(\varpi_m).$$

4 Numerical simulation results

The numerical simulation results presented in this section have been not only obtained in a record time through the choice of an efficient and fast method (RK4-IP) but also thanks to the kind help of Project team CORDIAL from IRISA (CNRS UMR 6074), it has been possible to run our simulations on a multi-core processing unit with 64 physically separated processors and 132 Go RAM. Hence it has been likely to optimize computation time by performing multi-threaded FFT, a routine for shared-memory parallel hardware handled by FFTW library [11]. This option was useful to save computation time since RK4-IP computations involved a time/frequency number of sampling points exceeding 2^{19}. Moreover, as explained in Section 3.3, generation and propagation of a large number of outcomes (≈2000) of the random process is required. Regarding this, an additive gain of time is possible through independent generation and simultaneous propagation of multiple outcomes of the random process, which appears as an alternative computation technique. Its features help to drastically reduce computing time. For instance, with a number of 2^{19} time sampling points the computing time for the generation and propagation of 2000 outcomes takes roughly 1 hour and a half through the parallel computation of 50 parallel outcomes, including an adaptive step-size control strategy with tolerance $\mathrm{tol} = 10^{-7}$ but without FFT multi-threading.

Some valuable physical statements can be deduced from numerical simulation experiments. Namely, important information regarding the impact of fiber linearities and nonlinearities on partially coherent (PC) laser source can be obtained. As well, the design of a PC laser source is made convenient since some of its physical features such as spectrum width and shape can be adjusted through the setting of the correlation function width and shape.

The simulation parameters used in this paper are related to the propagation and amplification of high-power (hundreds of Watts) PC super Gaussian pulse width $T_p = 0.5$ ns half-width into 3 m of Yb^{3+}-doped active fiber (booster) exhibiting an amplification gain ranging from 10 to 20 dB depending on the laser diode pump power. As mentioned in the Introduction, we want to investigate the impact of the PC source coherence time t_{coh} on its amplification.

Results depicted in Figure 2 show the outgoing mean power spectrum density (PSD) [21] after 3 m of propagation and 18.6 dB amplification ($P_{\mathrm{pump}} = 35$ W) in the booster for different values of the booster Kerr parameter γ ranging from 0.2 to 0.8 $\mathrm{W}^{-1}\ \mathrm{km}^{-1}$. The input mean PSD shape is Lorentzian and it corresponds to a complex Gaussian random process generated at a carrier frequency $\lambda_S = 1064$ nm with an exponential covariance function and a coherence time $t_{\mathrm{coh}} = 2.65$ ps. As the Kerr effect is increasing, PSD spreading and Raman shift tend to grow bigger.

The input field's covariance function is given by

$$\mathrm{C}_{A^{[z_n]}}(\tau) = \exp(-|\tau/t_{\mathrm{coh}}|).$$

By virtue of the Wiener-Khinchin theorem in the very special case of a wide-sense stationary complex random process, the covariance function and the PSD form a Fourier transform pair [21]. Hence, the input PSD (IN) is Lorentzian with a full width at half maximum (FWHM)

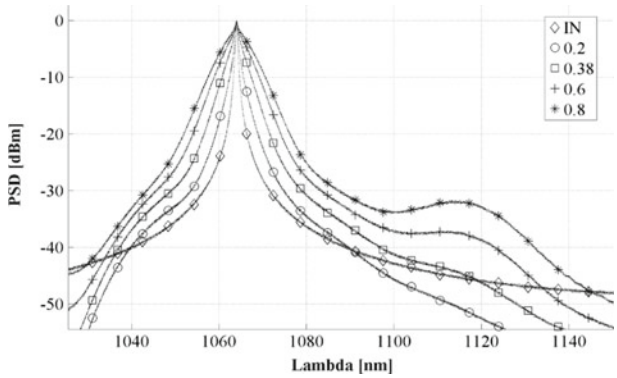

Fig. 2. fiber amplified PSD according to the fiber Kerr parameter γ ranging from 0.2 to 0.8 W^{-1} km^{-1}. IN stands for the Lorentzian input PSD.

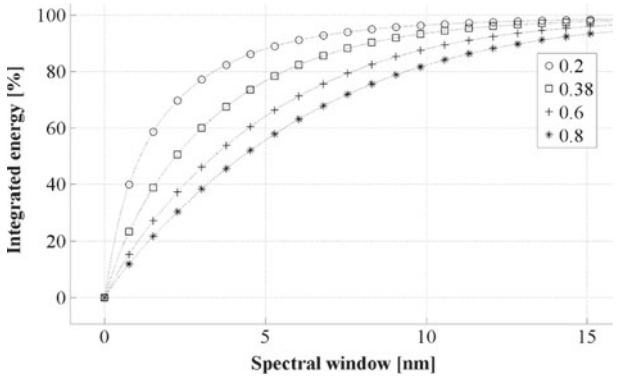

Fig. 3. Corresponding integrated DSP energy contained in the area centered at maximum spectrum power $\lambda_S = 1064$ nm for different values of fiber Kerr parameter γ ranging from 0.2 to 0.8 W^{-1} km^{-1}.

$\Delta\nu_{\mathrm{IN}}$ depending on t_{coh} through the relationship:

$$\Delta\nu_{\mathrm{IN}} = \frac{1}{\pi t_{\mathrm{coh}}}.$$

With an initial FWHM $\Delta\nu_{\mathrm{IN}} = 120$ GHz, we can appreciate in Figure 2 a noticeable behavior through propagation in active fiber. Our software allows not only to appreciate and quantify the PSD broadening around λ_S due to self-phase modulation (SPM), but also it allows the quantification of the Raman induced frequency shift (RIFS) which is made possible with the choice of a wide spectral window (200 nm) [2]. The RIFS is an inelastic phenomenon which appears as a transfer of energy from high-frequency components λ_S of a pulse to the lower-frequency components of the same pulse. Regarding our experimental setup (Fig. 1), Raman shift and SPM represent deleterious effects leading to spectrum broadening responsible for a decreasing efficiency at the frequency doubling stage. Thus, booster amplifiers and PC laser properties lead to more or less emphasize those nonlinearities. Regarding the Raman energy quantity, comparison with previous work [1] shows a lower quantity of energy. We suspect that numerical computation of Raman spontaneous energy added to amplified spontaneous emission can drastically increase the amount of spectral energy above 1100 nm.

A closer insight showed in Figure 3 completes the results presented in Figure 2 and certifies that the phenomenon of spectrum spreading is responsible for a poorer energy confinement as γ is increasing which is detrimental to an optimum frequency doubling. We can notify that energy confinement decreases proportionally with γ. Indeed, half of the output signal energy is confined into a 1 nm spectral window for $\gamma = 0.2$ W^{-1} km^{-1}, this same energy is confined into a 4 nm spectral window when γ is four times bigger.

Interesting behaviors can be quantified by modifying the coherence time of input complex random process. In Figure 4, as input PSD half-width is increased we have measured the output PSD enlargement $\eta = \Delta\nu_{\mathrm{OUT}}/\Delta\nu_{\mathrm{IN}}$ and the fraction of Raman energy considered as the total energy located at $\lambda > 1100$ nm. Both values increase in a monotonic way, however η does not increase linearly

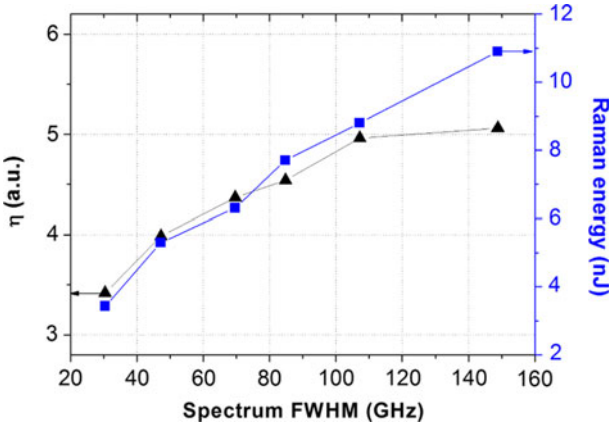

Fig. 4. Spectral spreading and corresponding integrated Raman energy at fiber output for a Lorentzian input spectrum shape with FWHM ranging from 30 to 150 GHz.

at the difference with the Raman energy fraction. As we can see, Kerr nonlinearities and Raman induced frequency shift have an appreciable impact on coherence properties through amplification and propagation. However, a close comparison between the modeling and experimental results shows a spectrum spreading and Raman energy which is far more important in the experimental case [1]. We believe that adding Raman spontaneous emission in our model should solve this mismatch.

Finally, Figure 5 shows the dependence of the PSD spreading on the choice of covariance function $C_{A^{[z_n]}}$. PSD enlargement η has been measured for increasing values of the laser diode pump power leading to a total linear amplification ranging from 11.9 to 18.6 dB. As the pump power increases, in both cases η is increasing too in a same way, however η is two times bigger with an exponential covariance function (Lorentzian spectrum). Hence, accurate experimental measurement of $C_{A^{[z_n]}}$ is necessary in order to quantify spectrum enlargement at booster output.

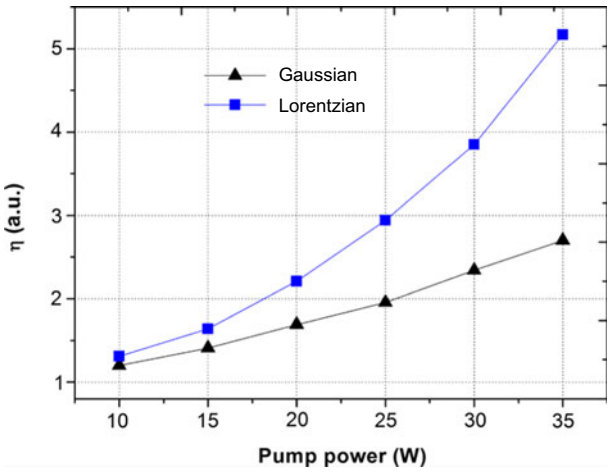

Fig. 5. Spectral spreading at fiber output for a respectively Gaussian and Lorentzian input spectrum shape with same FWHM of 130 GHz. The spectral spreading has been measured for an increasing pump power ranging from 10 to 35 W.

5 Conclusion

We have presented in this paper a numerical simulation approach dedicated to the generation of partially coherent laser source and its propagation into a fiber amplifier. We have demonstrated an implementation of the RK4-IP method for solving the generalized nonlinear Schrödinger equation. The method exhibits a fourth-order convergence and it is implemented together with an embedded Runge-Kutta method for adaptive step-size control. Partially coherent laser source are modeled by means of complex Gaussian random processes. The choice of the circular embedding method for the generation of complex Gaussian random processes allows the simulation of partially coherent laser sources over a sufficiently large number of time sampling points (up to 2^{23}) to ensure high accuracy and wide span investigation. Besides computing speed has been optimized by the use of multi-threading technique for FFT computing and by parallel running of independent Gaussian random processes. Our numerical results show the ability of our numerical simulation software to bring physical statement to a pragmatic research topic such as high-power nanosecond partially coherent pulse amplification in a 3 m Yb^{3+}-doped fiber. However, this numerical simulation software is for sure multipurpose and is able to carry out studies in different photonic areas such as supercontinuum generation, or to deal with telecommunication concerns like data format transmission or optic functions based on four wave mixing.

The authors would like to warmly thank Pr. O. Boëffard and Dr. S. Le Maguer from IRISA (CNRS UMR 6074) Project team CORDIAL for their illuminating conversations on computer science, technical support and computing skills. This work is supported by the Conseil Rgional de Bretagne in the framework of the Green Laser project.

References

1. P.B. D'Augères, A. Mugnier, D. Pureur, T. Chartier, in *Nonlinear Optics and Applications IV* (SPIE Photonics Europe, Bruxelles, Belgique, 2010), pp. 77280S–77280S
2. G. Agrawal, in *Nonlinear Fiber Optics*, 3rd edn. (Academic Press, San Diego, USA, 2001)
3. K. Okamoto, in *Fundamentals of Optical Waveguides*, 2nd edn. (Academic Press, San Diego, USA, 2006)
4. D. Hollenbeck, C.D. Cantrell, J. Opt. Soc. Am. B **19**, 2886 (2002)
5. R.H. Stolen, J.P. Gordon, W.J. Tomlinson, H.A. Haus, J. Opt. Soc. Am. B **6**, 1159 (1989)
6. O.V. Sinkin, R. Holzlöhner, J. Zweck, C.R. Menyuk, J. Lightwave Technol. **21**, 61 (2003)
7. T.N. Nguyen, M. Gay, L.T. Bramerie, T. Chartier, J.C. Simon, Opt. Exp. **14**, 1737 (2006)
8. J. Hult, J. Lightwave Technol. **25**, 3770 (2007)
9. S. Balac, A. Fernandez, F. Mahé, R. Texier-Picard, CNRS FOTON Technical Report, `http://hal.archives-ouvertes.fr` (2012)
10. J.C. Butcher, *Numerical Methods for Ordinary Differential Equations* (John Wiley and Sons, Chichester, England, 2008)
11. M. Frigo, S.G. Johnson, Proc. IEEE **2**, 216 (2005)
12. A. Heidt, J. Lightwave Technol. **27**, 3984 (2009)
13. S. Balac, A. Fernandez, CNRS FOTON technical report, `http://hal.archives-ouvertes.fr/hal-00740771` (2012)
14. J.R. Dormand, P.J. Prince, Celest. Mech. **18**, 223 (1978)
15. S. Balac, F. Mahé, Comput. Phys. Commun. **184**, 1211 (2013)
16. B. Gross, J.T. Manassah, Opt. Lett. **16**, 1835 (1991)
17. C.R. Dietrich, G.N. Newsam, Water Resour. Res. **29**, 2861 (1993)
18. A.T.A. Wood, G. Chan, J. Comput. Graph. Stat. **3**, 409 (1994)
19. G. Chan, A.T.A. Wood, Stat. Comput. **9**, 265 (1999)
20. D.B. Percival, Signal Process. **86**, 1470 (2006)
21. J.W. Goodman, *Statistical Optics* (Wiley Classics Library, New York, USA, 2000)